nature communications

Article | Article in Press

https://doi.org/10.1038/s41467-026-77489-x

Geometrical-optics resonator photonics

Received: 27 August 2025

Accepted: 13 August 2026

Published online: 14 September 2026

Check for updates

Chunlei Sun[1,2,6], Kangjian Bao[1,2,6], Boshu Sun[1,2], Bo Tang[3], Xu Yang[1,2], Zequn Chen[1,2], Yiheng Tang[1,2], Qingyan Deng[1,2], Yingchun Wu[1,2], Lei Liu[1,2], Renjie Tang[1,2], Zongxi Li[1,2], Kunhao Lei[4], Yilin Shi[1,2], William Shieh[1,2,5], Min Qiu[1,2,5], Hongtao Lin[4] & Lan Li[1,2,5]

Conventional waveguide optical resonators face inherent limitations of low damage thresholds, limited coupling tunability, and stochastic resonance. To overcome these, we introduce a geometrical-optics resonator (GOR) framework, emulating free-space reflection and thin-film coupling on-chip. Using ultra-wide waveguides with total internal reflection (TIR) mirrors and frustrated-TIR couplers, GORs eliminate conventional constraints. Fabricated devices achieve intrinsic Q-factors >1 million and enable tunable microwave photonic filters operating distortion-free at about 10× higher optical power. Design flexibility allows precisely tuned coupled resonators, facilitating cascaded networks for spectral engineering. Demonstrated GOR photonic molecules exhibit dynamically adjustable mode splitting (0.49 free spectral range), nearing theoretical limits. The platform also realizes record-large-scale Floquet topological photonic insulators with 1281 GOR lattices, supporting robust edge modes against defects and a broadband continuum. The GOR sets new performance benchmarks, enabling scalable platforms for quantum simulation and topological networks while driving integrated photonics toward higher density and system-level integration.

Optical resonators, pivotal in modern photonics, come in various types, including spatial Fabry-Pérot cavities and crystalline whispering-gallery-mode resonators. Among them, on-chip integrated resonators stand out as a compact and scalable solution that seamlessly integrates with semiconductor manufacturing processes as the backbone of photonic integrated circuits (PICs). They bridge classical and quantum photonics, enabling nanoscale light manipulation and driving advances in optical communication[1], sensing[2], computing[3], and memory[4]. On-chip resonators, primarily in the form of microrings or photonic crystal cavities, are typically constructed with single-mode waveguides that have subwavelength or wavelength-scale dimensions. They rely on evanescent field coupling via directional couplers to transfer light between waveguides and resonators. While this design is a widely adopted classic and has become a cornerstone in integrated optics, these resonators still face certain intrinsic limitations, such as a low waveguide optical damage threshold, limited coupling tunability, added propagation losses due to waveguide sidewall roughness, and instability of the resonance condition due to random phase errors.

To mitigate these issues, researchers have turned to multi-mode waveguides as an alternative to single-mode waveguides[5–7]. Due to the relatively large waveguide widths and weak interaction between light and the waveguide edges, scattering losses and random phase errors are suppressed, achieving high-Q microcavities over one million[5–7]. However, these conventional waveguide optical resonators (WORs) still exhibit a very strong localization of the optical field. Under high-power and high-Q conditions, strong optical and thermal nonlinear effects can cause distortion of the transmitted signal and even damage the waveguide. High-performance resonators based on

[1]Zhejiang Key Laboratory of 3D Micro/Nano Fabrication and Characterization, Department of Electronic and Information Engineering, School of Engineering, Westlake University, Hangzhou, China. [2]Institute of Advanced Technology, Westlake Institute for Advanced Study, Hangzhou, China. [3]Institute of Microelectronics of the Chinese Academy of Sciences, Beijing, China. [4]State Key Laboratory of Brain-Machine Intelligence, College of Information Science and Electronic Engineering, Zhejiang University, Hangzhou, China. [5]Westlake Institute for Optoelectronics, Hangzhou, China. [6]These authors contributed equally: Chunlei Sun, Kangjian Bao. e-mail: sunchunlei@westlake.edu.cn; qiumin@westlake.edu.cn; hometown@zju.edu.cn; lilan@westlake.edu.cn

low-index-contrast materials such as low pressure chemical vapor deposition (LPCVD) SiN can achieve ultra-high Q factors and damage thresholds but are difficult to be compatible with mainstream active SOI platforms[8]. While plasma-enhanced chemical vapor deposition (PECVD) SiN resonators provide foundry-compatible integration with SOI platform, they typically exhibit propagation losses exceeding 0.5 dB/cm in the communication band unless subjected to high-thermal-budget annealing processes[9,10]. Additionally, multi-mode waveguides present challenges in flexible photonic circuit design due to modal complexity and crosstalk, which complicate mode-selective routing. Furthermore, their inter-waveguide coupling strength is often weaker than that of single-mode counterparts, due to the reduced spatial overlap of evanescent fields. Typically, the mode coupling in coupled optical microcavity systems like photonic molecules and topological photonic insulators (TPIs), is proportional to the ratio of the coupling strength to the round-trip length of the resonator[11]. Consequently, limited coupling and large-sized optical resonators obscure mode coupling, such as spectral splitting in photonic molecules. In addition, TPIs have non-trivial bandgaps that emerge under conditions of strong coupling, typically exceeding 0.5[12], where conventional WOR framework faces difficulties, raising the urgent need for innovative resonator architectures that unite high damage thresholds, flexible coupling control and resonance stability in on-chip resonators, which is essential to propel breakthrough in microwave photonics[13], quantum technology[11], and communication systems[14].

In this work, we present a transformative solution using on-chip geometrical-optic resonator (GOR) photonics, which revolutionizes light coupling and resonance mechanisms through principles such as total internal reflection (TIR) and frustrated total internal reflection (FTIR), enabling far-reaching applications in areas from microwave photonics to topological photonics, as shown in Fig.1a. Although prior methodologies have applied geometrical optics to optical filter design[15] and mode multiplexer[16,17], fundamental limitations persisted due to intermodal coupling, which prevents the observation of high-Q resonance. Our pioneering GOR framework extends geometrical optics to ultra-wide waveguides (with widths of tens of wavelengths) to suppress beam divergence and the Goos-Hänchen shift, enabling unprecedented stability of on-chip mode control. The framework can nearly perfectly mimic the total reflection of free-space light at high refractive index contrast interfaces, as well as the coupling observed in multilayer films[18]. Consequently, it effectively reduces both intermodal coupling and scattering losses, and minimizes random phase errors. This architecture achieves intrinsic Q-factors >1 million with a finesse of 233 as valuable integrated photonic components. Key demonstrations include: (1) a single GOR enabling a 35.6-GHz tunable integrated microwave photonic filter (IMPF) without signal distortion at high optical pump power; (2) photonic molecules with dynamically adjustable mode splitting, nearing the theoretical limit of photonic molecules; and (3) a record-large-scale Floquet TPI (FTPI) utilizing periodic modulation to achieve backscattering-free and defect-immune topological transport with 1281 GOR lattices.

Results

Unveiling the mechanism for high-Q geometrical-optics resonator

Conventional WORs rely on micrometer-scale waveguides, where propagation loss mainly stems from scattering due to sidewall and surface roughness, which diminishes as the waveguide width increases. In contrast, our design features ultra-wide waveguides, one to two orders of magnitude broader than conventional ones (Fig. 1b). This significantly reduces light–sidewall interactions, thereby cutting random phase errors and propagation loss (Supplementary Note 1). However, wider waveguides complicate light turning due to longer round-trip paths and make directional coupling more challenging. The evanescent wave's effectiveness, depends on proximity to the waveguide center, influenced by both waveguide width and inter-waveguide spacing. To tackle these issues, we replace conventional bent waveguides with TIR mirrors and conventional directional couplers with FTIR couplers. The TIR mirrors, leveraging the high refractive index contrast of the Silicon-On-Insulator (SOI) platform, reduce bend loss to 0.0025 dB per mirror at a 50-μm waveguide width (Supplementary Note 2). The FTIR couplers are highly efficient, mainly affected by waveguide spacing but largely insensitive to width variations due to thin-film interference (Supplementary Note 3)[19]. For connecting to narrow waveguides, we employ a parabolic mirror-based mode spot converter (MSC) with a low loss of 0.18 dB (Supplementary Note 4), which is primarily limited by mode-field mismatch compounded by non-ideal beam broadening and can be improved by optimizing the parabolic mirror profile to minimize aberrations.

Figure 1c shows the calculated intrinsic Q-factor (Q_i). Details of Q-factor estimation can be found in the Methods section. Note that the waveguide sidewall etching profile also affects the scattering at the TIR mirror, further discussed in Supplementary Note 2. Fortunately, the SOI platform features nearly perpendicular waveguide sidewalls, substantially lowering the loss associated with each bend. The Q-factor can easily exceed one million by choosing a proper round-trip length and increasing the waveguide width. Figure 1d shows the scanning electron microscope (SEM) images of MSC and FTIR coupler. The optical resonance within the fabricated silicon GORs was successfully captured by imaging the scattered light at resonant wavelengths, as illustrated in Fig. 1e (see Methods for further details).

Demonstration of the ultra-wideband tunable integrated microwave photonic filter

Figure 2a presents the measured spectral responses at the through port of the GORs with $W_d = 50$ μm. Figure 2b provides the transmission spectra for resonant peaks around 1541 nm, showing a high Q_i of 1.35×10^6. Conventional WORs enhance light-matter interactions through high Q-factors and small mode volumes, yet thermal effects such as bistability, can cause undesired nonlinear spectral distortions and even waveguide damage. GORs maintain high Q-factors and reduce power density by widening waveguides, which lowers the peak intensity at the waveguide center by 32.6 times compared to a 1.5 μm-wide multimode waveguide (Supplementary Note 5). GORs achieve significant improvements in thermal stability, nonlinearity suppression, and damage threshold. Specifically, GORs show 9.0 dB higher thermal resilience than WORs (Fig. 2c) (Supplementary Note 5). Given their similar cavity lengths and higher Q-factor, GORs can support an order of magnitude higher optical pump power than WORs.

Furthermore, we employed IMPF methods to validate the Q_i of the GOR (setup shown in Fig. 2d, details in Methods section). Figure 2e reveals a single passband of the proposed MPF with a Lorentzian fit curve indicating a 3-dB bandwidth of 339 MHz, corresponding to a Q_i of approximately 1.14×10^6. We also realized a tunable IMPF with an impressively broad tuning range of over 35.6 GHz, extending from the L-band to the Ka-band (Fig. 2f). At an input on-chip pump power of approximately 11 dBm, no visible signal distortions were observed.

Static photonic molecules utilizing geometrical-optics resonators

Photonic molecules[20,21], simulate mode hybridization behavior to exhibit discrete optical energy levels, making them an ideal platform for studying novel quantum optical phenomena and control methods such as Rabi oscillations and the Stark effect[22,23]. Moreover, precise control of phase and energy in photonic molecules enables frequency and phase matching in dispersion engineering, which is crucial for applications including spectrometer[24,25], exceptional point (EP) manipulation[26], stimulated Brillouin lasers[27,28] and Kerr combs[29].

https://doi.org/10.1038/s41467-026-77489-x

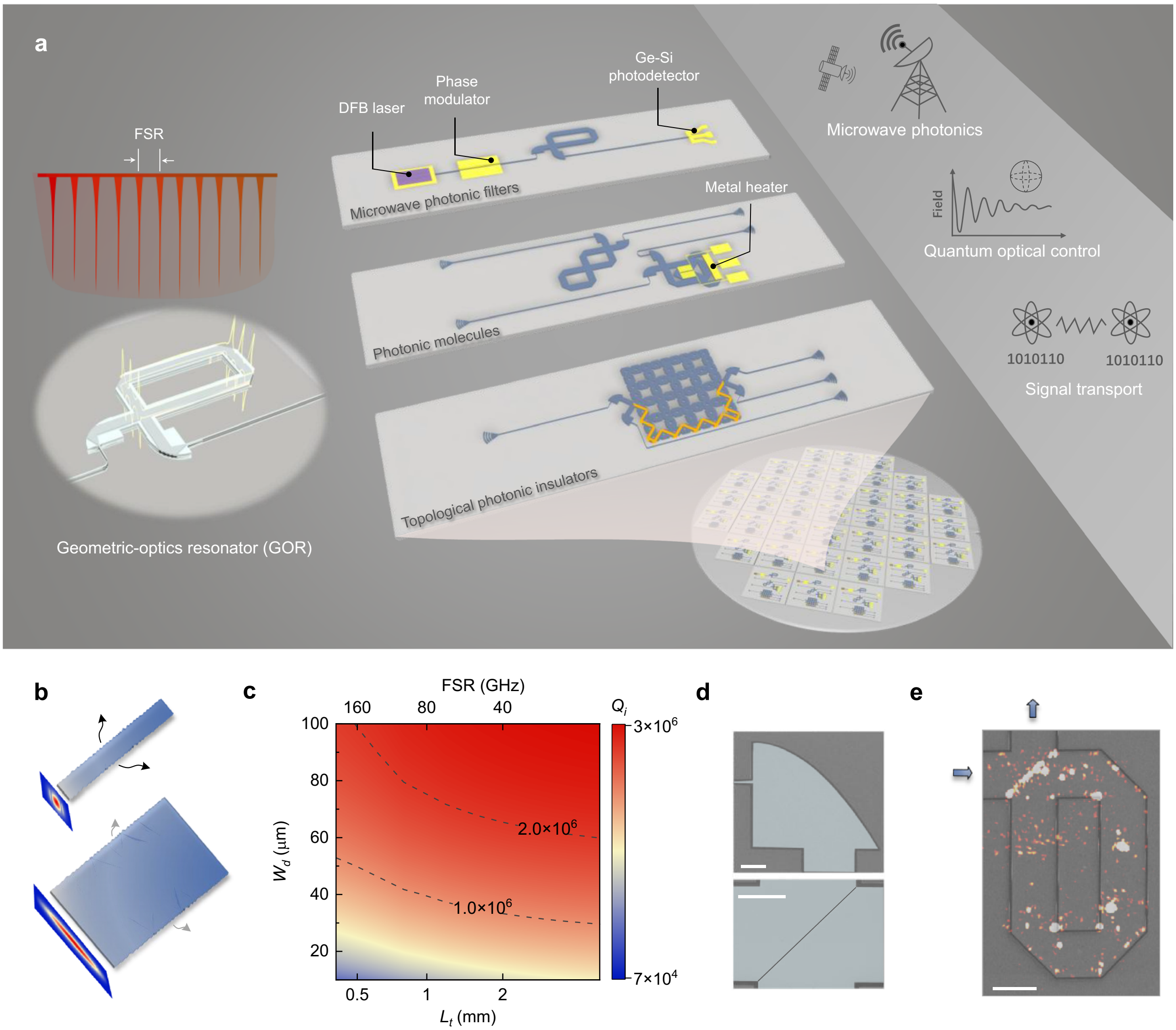

Fig. 1 | On-chip geometrical-optics resonator photonic platform. a Conceptual diagrams of on-chip high-*Q* GOR-based devices and their potential applications in integrated microwave photonic filters, static and dynamic photonic molecules, and FTPI. The inset shows a 3D view of the GOR. **b** Comparison of waveguide sidewall geometries: narrow conventional design with intense scattering radiation and proposed ultra-wide waveguides with reduced scattering. **c** Calculated Q_i with varying waveguide widths W_d and round-trip lengths L_t. The waveguide sidewall and surface roughness are considered, and the sidewall angle of the TIR mirror is set to 90°. **d** Colorized SEM images of MSC and FTIR coupler. Scale bar, 25 μm. **e** Colorized infrared images of real-space electromagnetic field distribution at resonant wavelength within the GOR are visualized by an infrared camera and are superimposed on a SEM image. Scale bar, 50 μm. The noise outside the GOR originates from stray light that has not been coupled into the waveguide, reflected by the chip and optical fiber into the camera.

When optical resonators are placed close together, the evanescent field of one perturbs the adjacent resonator, causing linear coupling. This interaction eliminates frequency degeneracy and results in normal mode splitting, yielding a frequency doublet (Fig. 3a). Assuming negligible losses, the frequency difference, Δ, associated with the mode splitting is given from a temporal coupled-mode theory (T-CMT) model[30]:

$$\Delta = \sqrt{(\delta\omega)^2 + 4\mu^2} \tag{1}$$

where μ represents the coupling rate between the resonator modes. The terms δω refer to the resonant angular frequency difference of the resonator modes in the absence of coupling. See Supplementary Note 6 for the details of T-CMT model. The photonic molecule provides a pair of optical energy levels, as depicted in Figs. 3b and 3c. At power coupling strength $K = 1$, which represents complete optical coupling, the mode splitting reaches half a free spectral range (FSR/2). This signifies the integration of the two individual resonators into a composite resonator with a doubled round-trip length, as illustrated in Fig. 3d.

The conceptual diagram of photonic molecules comprising two GORs that have the same round-trip length and are separated by a coupling gap *G* are shown in Fig 3e. This photonic molecule supports both a low-frequency symmetric mode and a high-frequency antisymmetric mode. Figure 3f displays the measured spectral responses at the through port for the photonic molecules with coupling gaps of 70, 140, and 210 nm and FSR of 1.06 nm. A more pronounced splitting effect is observed for smaller coupling gaps. Figure 3g provides the transmission spectra near 1541 nm. In addition, optical coupling within resonators can be achieved by introducing grating structures, but this often requires challenging nanoscale fabrication[31–35]. Ultra-wide waveguides, with larger mode volumes, reduce edge-light interaction,

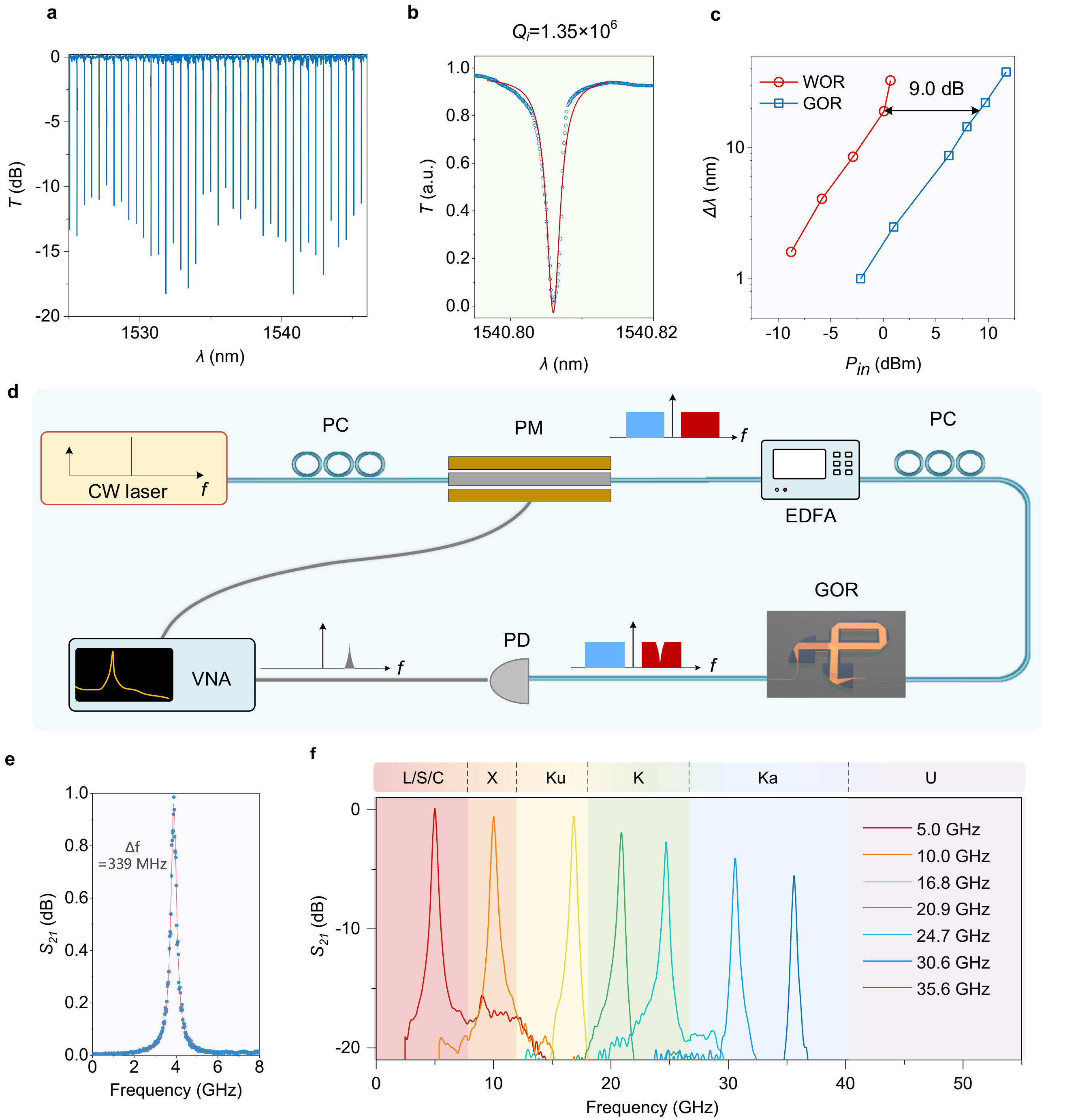

Fig. 2 | Characterization of single geometrical-optics resonator and tunable integrated microwave photonic filter demonstration. **a** Measured spectral responses at the through port of the fabricated silicon high-Q GORs. **b** Linear transmission spectra around the resonant peaks with the Lorentzian model fitting show the $Q_i = 1.35 \times 10^6$. **c** Resonance wavelength shift ($\Delta\lambda$) of GOR (blue) and WOR (red) as a function of input pump power (P_{in}). **d** Schematic diagram of the IMPF, employing distinct colors (red and blue) to denote the π phase difference between the two sidebands. **e** Measured normalized S_{21} transmission response using the GOR as a high-resolution microwave photonic band-pass filter. The 3-dB bandwidth is 339 MHz. **f** Measured normalized S_{21} transmission response of the IMPF, spanning from the L band to the Ka band. PC polarization controller. PM phase modulator. EDFA Erbium-doped fiber amplifier. PD photodetector. VNA vector network analyzer.

allowing larger structure perturbations and easing fabrication. Figure 3h shows a single-resonator photonic molecule with Bragg gratings (Fig. 3i) exciting counter-propagating higher-order modes (see Methods). The grating details (Fig. 3j): period 275 nm, amplitude 500 nm, 800 periods. Figure 3k displays the measured spectral responses of the fabricated grating-assisted photonic molecules.

Dynamic photonic molecules with extensively tunable mode-splitting control

Dynamic photonic molecules can achieve tunable mode splitting through adjustable resonator-resonator coupling. If the power coupling strength K can be tuned from 0 to 1, the photonic molecule can realize fully tunable mode-splitting across a range of FSR/2. To date, substantial efforts have been exerted to achieve dynamic photonic

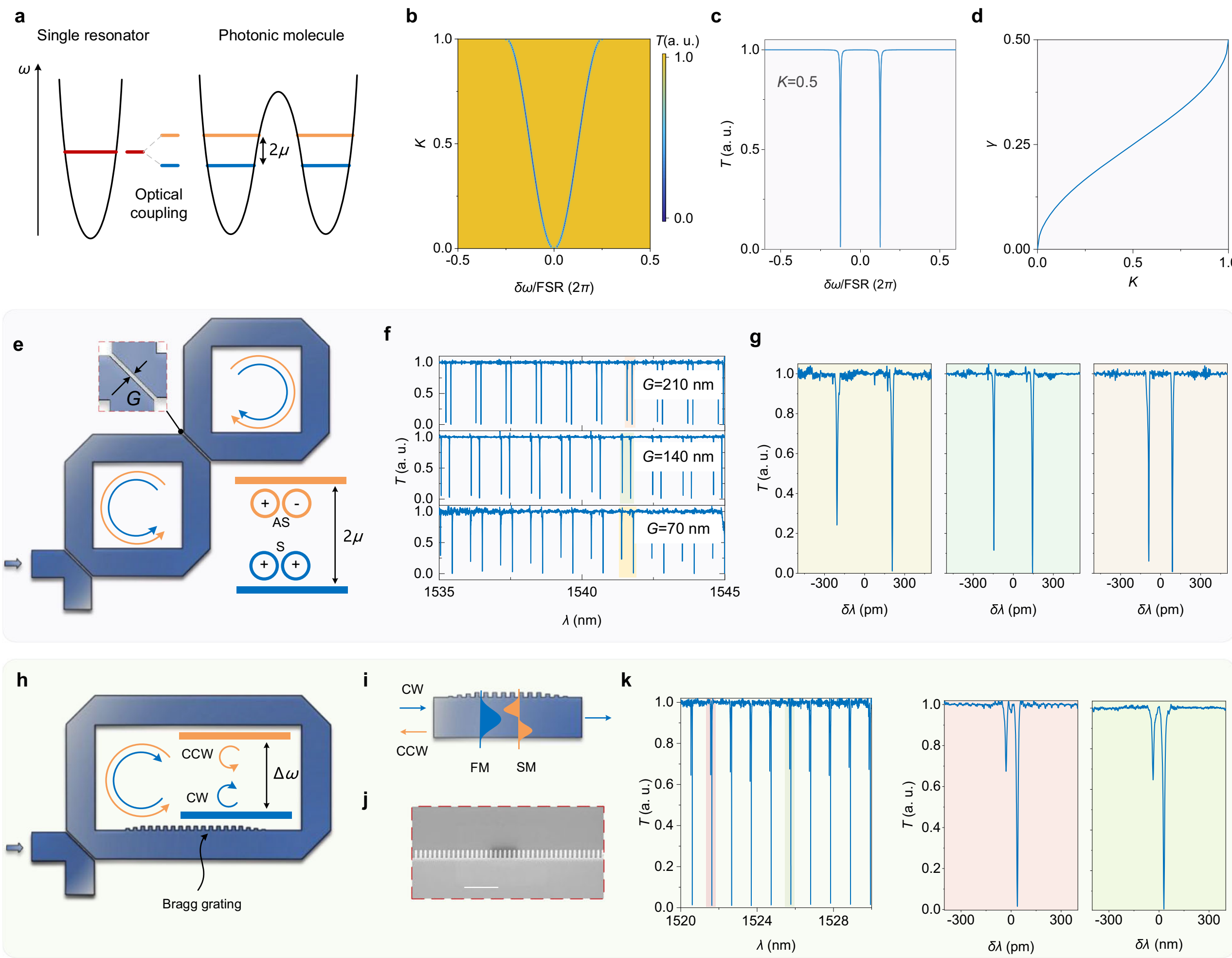

Fig. 3 | Designs and characteristics of static photonic molecules based on geometrical-optics resonators. a Photonic molecules formed by a pair of identical coupled optical resonators with the same resonant frequencies. The coupling effect induces a controllable resonance splitting, μ, akin to the split energy levels observed in a diatomic molecule. **b** Simulated transmission spectra of the photonic two-level system are presented, showing the variation in power coupling strength K and frequency detuning $\delta\omega$ normalized by FSR. **c** Simulated transmission spectra reveal that the two optical modes are separated by FSR/4 in the case of $K = 0.5$. **d** Normalized mode splitting $\gamma = 2\mu/(2\pi\times\text{FSR})$ experiences a transition from 0 to 0.5 as K increases from 0 to 1. **e** Photonic molecules generated with a pair of identical coupled GORs, where coupling is induced by placing them in close proximity. The system features two distinct energy levels: symmetric (S) and antisymmetric (AS) optical modes, denoted by the blue and orange lines, respectively. **f** Measured spectral responses at the through port of the fabricated silicon photonic molecules with an FSR of 1.06 nm are presented for coupled gaps of 70, 140 and 210 nm. **g** Transmission spectra around 1541 nm for the three different coupled gaps, with the background colors matching those indicated in (**f**). **h** Bragg grating is introduced into the GOR as a mode converter to enable coupling between the clockwise (CW) and counter-clockwise (CCW) modes, thereby forming a single-resonator photonic molecule. **i** Mode converter based on a lateral waveguide Bragg grating. When the first-order mode (FM) encounters a discontinuity, a portion of the power is coupled into the second-order mode (SM) with an opposite propagation direction7. **j** SEM image of the Bragg grating. Scale bar, 2 μm. **k** Measured spectral responses of the fabricated grating-assisted photonic molecules.

molecules[24,36–39]. However, real-time adjustment of the coupling strength between on-chip resonators over a large tuning range presents formidable challenges. One solid-state tuning method is to alter the spatial mode coupling within the resonator to create perturbations[37], but these are usually subtle to balance coupling strength and losses, thus limiting the mode-splitting range to much less than FSR/2.

Our proposed dynamic photonic molecule uses an asymmetric Mach-Zehnder interferometer (AMZI) to connect two GORs, enabling dynamic coupling (Fig. 4a). Detailed structure parameters are given in Supplementary Note 7. Like a conventional MZI based on a multimode interferometer (MMI) coupler, our proposed AMZI consists of two FTIR couplers connected by ultra-wide waveguides, as shown in Fig. 4b, which allows for the thermal control of the phase difference between its two arms. The power coupling efficiency K_T of AMZI is given by $K_T = 2K(1\text{-}K)(1+\cos(\Delta\varphi))$, where $\Delta\varphi$ is the phase difference between the two arms. When the power coupling strength K of the FTIR couplers is 0.5, adjusting $\Delta\phi$ can vary K_T between 0 and 1, enabling mode splitting across the entire tuning space (Fig. 4c). The AMZI's FSR is designed to be 3.45 nm to decrease the power consumption. Figure 4d shows the measured transmission spectrum of the AMZI-assisted photonic molecule with no bias voltage. Different mode splittings are observed within several adjacent FSRs. Scanning Microheater 2 alone pulls the resonant wavelengths of the two GORs in opposite directions, primarily through wavelength detuning, resulting in the characteristic avoided crossing curve (Fig. 4e, f). Scanning Microheater 1 while adjusting Microheater 2 to compensate for frequency shifts achieves the V-shaped curve (Fig. 4g, h). When Microheater 2 is at 0 mw and the phase difference $\Delta\varphi$ is 0, there is no mode splitting, corresponding to the minimum $K_T = 0$. At 384 mW for Microheater 2 and $\Delta\phi \approx \pi$, the splitting reaches its maximum of 0.286 nm (35.8 GHz), nearly half of the GOR's FSR of 0.585 nm

 https://doi.org/10.1038/s41467-026-77489-x

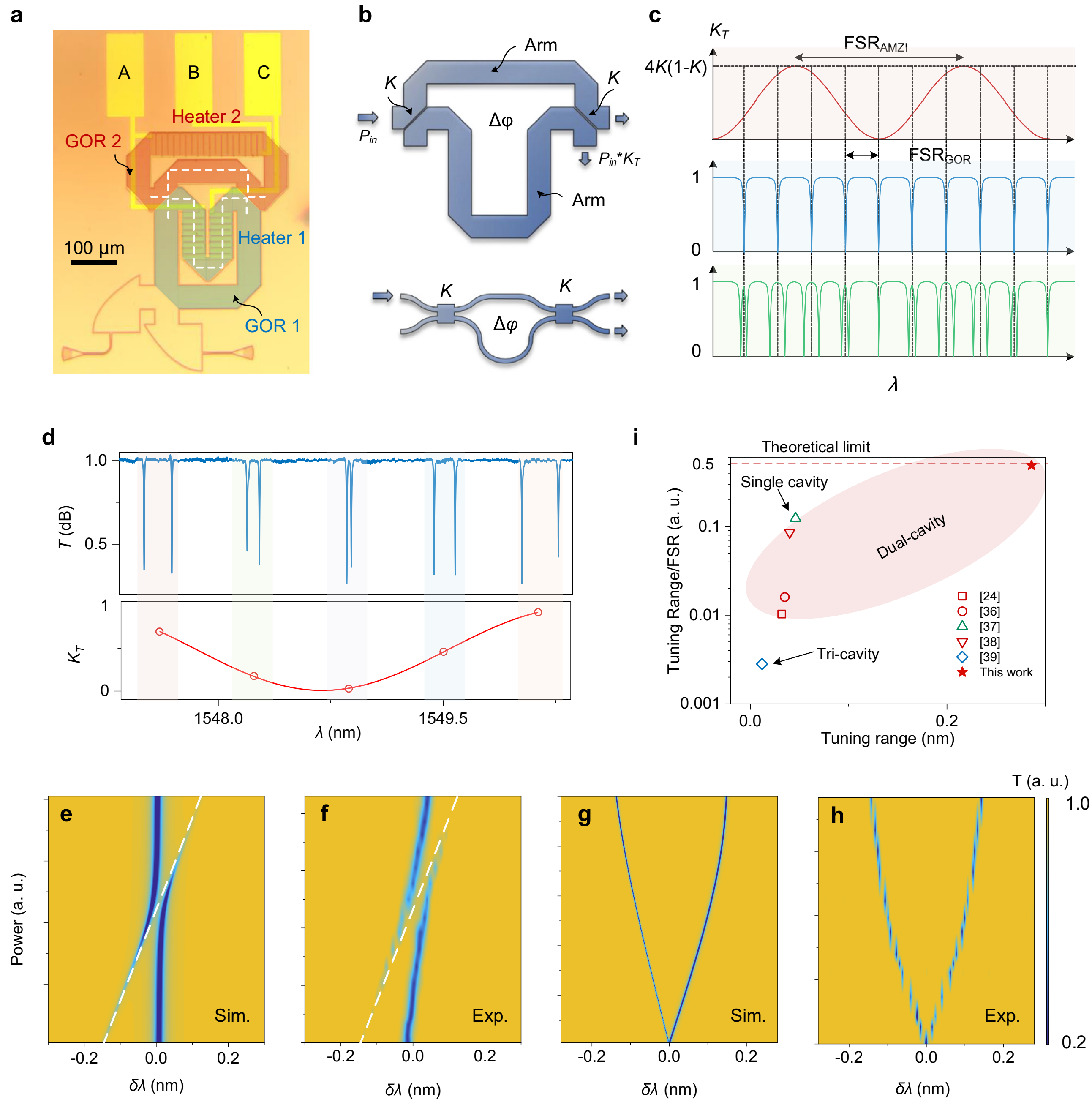

Fig. 4 | Extensively tunable mode-splitting control in the dynamic photonic molecule. a Optical image of the fabricated dynamic photonic molecule. Microheaters 1 and 2 are placed over GOR 1 (blue shaded area) and GOR 2 (red shaded area), respectively. An AMZI is introduced to enable varied optical coupling strength as a function of wavelength, as indicated by the white dashed lines. **b** Schematics of AMZIs based on FTIR couplers (top) and MMI couplers (bottom). **c** Illustration of the working principle of the tunable mode-splitting manipulation based on AMZI-assisted photonic molecules. Upper, middle and lower panels refer to the spectral response of AMZI, single GOR and AMZI-assisted photonic molecules, respectively. **d** Measured transmission spectrum of AMZI-assisted photonic molecules with no bias voltage (top). Calculated power coupling efficiency K_T of AMZI (bottom). Simulated (**e**) and measured (**f**) results of mode splitting as a function of heater power of Microheater 2. Simulated (**g**) and measured (**h**) results of mode splitting as a function of heater power of Microheater 1. **i** Summary of the performance of different schemes of dynamic photonic molecules. The red dashed line refers to FSR/2, which is the theoretical limit of the photonic molecule.

(73.1 GHz). To improve tuning efficiency and mitigate thermal crosstalk, efficient thermal confinement designs, such as etched deep trenches can be used[40]. To benchmark our dynamic photonic molecule, we compared it with existing works (Fig. 4i). By integrating an AMZI coupler, we achieved highly efficient and straightforward dynamic control with an impressively wide tuning range of up to 0.49 FSR, approaching the theoretical limit of FSR/2.

Floquet topological photonic insulators based on tri-resonator geometrical-optics resonator unit cells

FTPIs are a class of photonic lattices that possess the unique ability to support edge modes within their topologically protected bandgaps. These edge modes are a hallmark of topological phases, enabling a wide range of potential applications, including disorder-robust delay lines[41], quantum optical transport and generation[42,43]. However, most FTPI systems also support delocalized bulk modes, which can terminate edge modes within the bulk bands, narrowing their usable range. Additionally, random phase errors in the lattice diminish its disorder resistance, and strong perturbations can disrupt edge modes[44,45]. Typically, the weaker the coupling strength, the less robust the edge modes are against random phase errors. Conventional WORs either suffer from significant random phase errors due to single-mode waveguide sidewall roughness and fabrication errors, or lack sufficient coupling in multimode waveguides, both of which degrade the performance of FTPIs. Here, we introduce GOR into the FTPI with a tri-resonator model, which has become an advantageous model for studying FTPIs[46–48]. By employing an ultra-wide waveguide, giving it good robustness of edge modes against random phase errors (Supplementary Note 1).

In the periodic lattice structure, GORs primarily exist as site GORs and link GORs. Site GORs form the lattice backbone, defining its structure, while link GORs connect adjacent site GORs. Figure 5a illustrates an FTPI composed of a 5×5 site GOR lattice, with the tri-resonator GOR unit cell depicted in Fig. 5b. To miniaturize the FTPI and broaden the bandwidth of the edge modes, the width of the waveguide is set to $W_d = 20\,\mu m$, achieving a FSR of 5.3 nm. A subwavelength grating incorporated into the FTIR coupler is used to enhance coupling strength (Fig. 5c), with K_{sw} adjustable from 0 to 1 by tuning the grating duty cycle and coupling spacing (Supplementary Note 8). Figure 5d displays the theoretical transmission spectra at the drop port when coupling parameter θ is finely tuned from 0 to $\pi/2$. Adjusting θ and crossing the critical threshold of topological phase transitions (TPTs) at $\theta \approx 0.364\,\pi$, we observe the bandgap closing and reopening, eliminating topological edge modes in bandgap A. This phenomenon signifies a phase transition from a topological phase to a trivial one. The regions of flat and high transmission indicated by the dashed lines represent the FSR associated with the topological edge modes. Figure 5e, f display simulated/measured spectra before and after the TPT. By choosing θ, we trace the TPT experimentally, from topological edge modes (Fig. 5g) to disordered bulk modes in band A (Fig. 5h). Figures 5g, i illustrate the persistent presence of edge modes in bandgap B, enhanced in strong coupling cases. Figure 5j depicts the forbidden bandgap under strong coupling. Figure 5k examines the topological robustness against structural defects by removing a GOR lattice. In addition, an all-flat-band FTPI with a broad edge-mode continuum spanning multiple FSRs is observed when the coupling gap G is set to zero (Supplementary Note 9).

Discussion

In this paper, we propose an on-chip GOR architecture that redefines the design principles of optical resonators in integrated photonic systems by merging on-chip waveguide optics with classical geometrical optics theories. By using specialized waveguide geometries such as beam-width expansion, TIR mirrors, and FTIR couplers, our design overcomes the limitations of traditional photonic structures. This results in low-loss and low-random-phase-error propagation, high damage power threshold, and flexible layouts with a wide coupling strength tuning range. Moreover, the GOR architecture is material-agnostic, and its design principles are directly transferable to platforms such as SiN using standard etching processes to form the necessary trenches for achieving the TIR condition[49]. Our work establishes a versatile on-chip high-Q GOR framework applicable to single-resonator microwave photonic filters (enhancing thermal stability and nonlinearity suppression), dual-resonator photonic molecules (with flexible coupling tunability), and multi-resonator topological systems (robust edge modes against random phase errors and defects). Therefore, this framework is not only applicable to SOI but can also be directly transferred to advanced platforms like SiN, which offer lower loss and higher nonlinear damage thresholds, thereby providing a highly promising general solution for developing next-generation high-performance integrated photonic devices.

Such GORs with high thermal stability, nonlinearity suppression, and damage threshold could revolutionize microwave photonic systems. They can improve phase noise suppression and dynamic range, facilitating next-generation terahertz communication and ultra-precise photonic radar[13]. Leveraging its high Q-factor, GOR enables high-power self-injection-locked silicon lasers, traditionally based on wide-bandgap materials like silicon nitride[8,50]. The high Q-factor prolongs photon lifetime, narrowing the laser linewidth, while the high damage threshold mitigates thermally induced frequency shifts and photothermal damage, ensuring long-term stability in high-power applications. Moreover, dynamic photonic molecules with tunable mode splitting can achieve phase matching in optical nonlinear processes, such as stimulated Brillouin scattering (SBS), thereby addressing the narrow linewidth challenge[51].

By leveraging subwavelength grating-assisted FTIR couplers, we can easily achieve high coupling efficiency (>95%) across broad bandwidths. This efficiency is ideal for exciting stable topological boundary states in TPIs, even in disordered environments. Therefore, our proposed approach holds great potential for scaling up to ultra-large-scale topological photonic networks. We constructed a large-scale FTPI device with a 21×21 site GOR lattice (Supplementary Note 10). Within an area of $0.88 \times 0.88\,mm^2$, 1281 GORs were monolithically integrated. The width of the waveguide W_d was chosen to be 10 µm, with a round-trip length of 60 µm. To our knowledge, this is the largest and most densely integrated on-chip 2D FTPI to date. The two broad, flat plateaus within a single FSR in Fig. 5l signify high transmission efficiency of topological edge modes, while low-transmittance dips indicate energy loss from bulk states. The electromagnetic field distribution of the edge mode is shown in Fig. 5m. Notably, the device is highly immune to certain defects and disorders, as seen in complex structural defects arranged in a WLU shape created by removing multiple GORs (Fig. 5n). Further details are shown in Fig. S12. This improvement enables more stable signal transmission, parallel multi-channel photonic signal processing, high-power TPI lasers[44,52], and promotes the emergence of novel phenomena, such as topological solitons[53] and higher-order topological states[54].

Methods

Quality factor estimation for geometrical-optics resonator devices

The intrinsic quality factor Q_i is estimated using the formula $Q_i = \omega_0/2\gamma_i$, where ω_0 is the resonant angular frequency of light, and γ_i is the decay rate related to the intrinsic power loss, primarily stemming from waveguide scattering and bending losses. The decay rate γ_i is connected to the round-trip efficiency η of the optical resonator, which is given by the relationship $\eta = \exp(-\gamma_i n_g L_t/c)$, with c being the speed of light in a vacuum, and n_g the group refractive index. The round-trip efficiency encompasses both the ultrawide waveguide propagation loss and the bend loss of the TIR mirrors.

Experiment setup for tunable integrated microwave photonic filter measurement

Continuous wave (CW) light generated by a tunable laser (Santec TSL-550-C) is directed into a phase modulator through a polarization controller (PC) to optimize the polarization of the light. The RF signal is modulated onto the continuous-wave light by a high-speed commercial phase modulator (PM, iXBlue MPZ-LN-40), creating two optical sidebands with a π phase difference. The PM has a 3-dB electro-optic bandwidth of 40 GHz. The phase-modulated signal is then fed into the TIR-MR to convert phase modulation into intensity modulation. One of the sidebands is filtered out by the TIR-MR, and the two asymmetric sidebands will beat at the photodetector (PD, Anritsu MN4765B). The recovered RF signal is characterized by a vector network analyzer (VNA, Anritsu MS4647B). Thus, the processed optical response is mapped to the microwave domain.

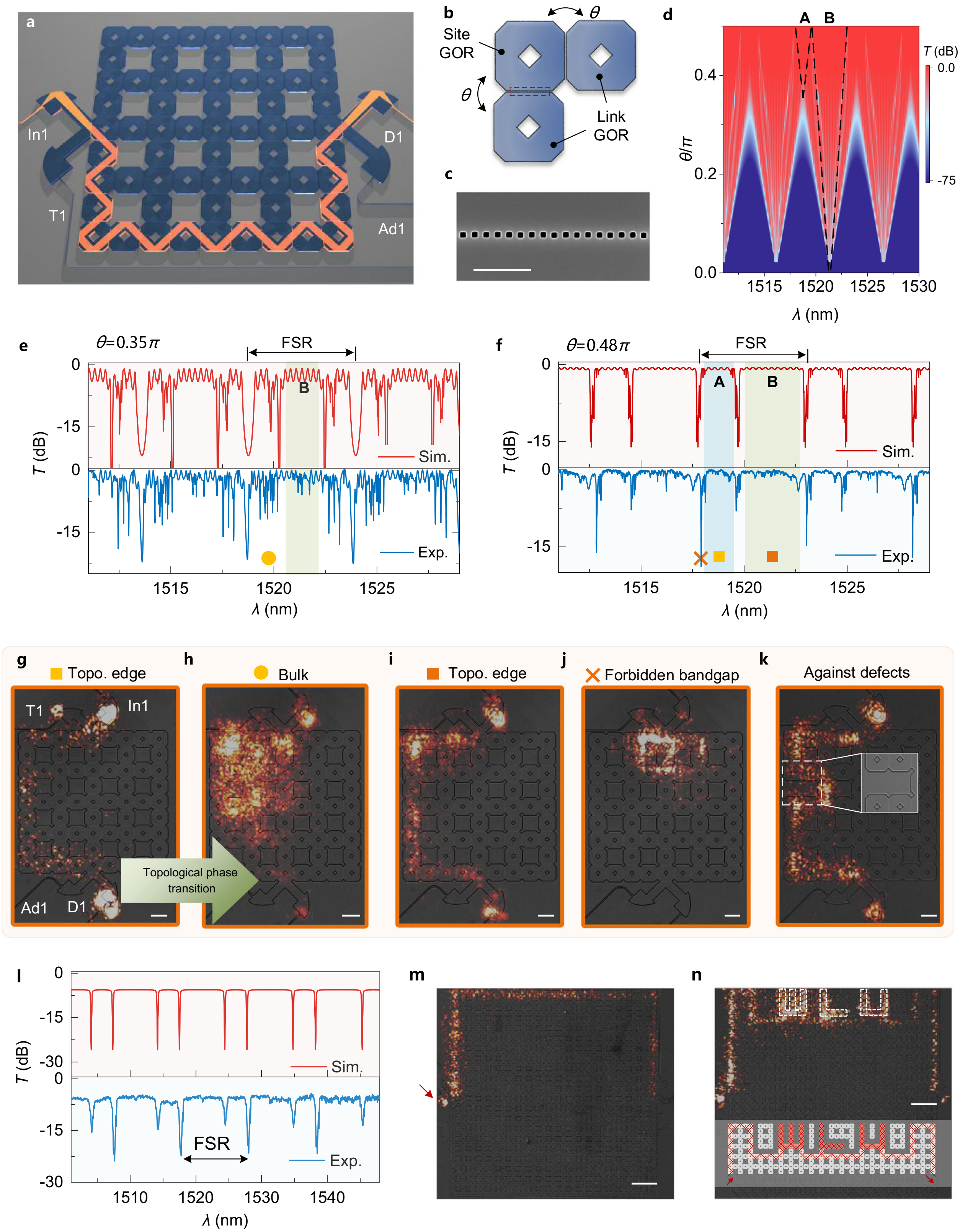

Fabrication of geometrical-optics resonator-based devices

We employed two distinct fabrication methods for the development of GOR-based devices. The single-ring GORs were fabricated using the 180-nm silicon photonic process at the Institute of Microelectronics of the Chinese Academy of Sciences (IMECAS). The fabrication process involved defining the waveguide patterns using deep ultraviolet (DUV) photolithography, followed by silicon etching via inductively coupled plasma (ICP) etching. For the photonic molecules and multi-resonator topological systems, electron beam lithography (EBL) was utilized for pattern definition since narrower coupling gaps and subwavelength gratings were adopted, and single-step ICP dry etching was employed to complete the 220-nm-thick silicon etching process. Subsequently, a

Fig. 5 | Geometrical-optics resonator-based Floquet topological photonic insulators. a Tri-resonator model as a framework for FTPI consisting of 5×5 site GOR lattices. **b** Schematic diagram of the tri-resonator unit cell based on GOR with power coupling parameter θ. **c** SEM image of subwavelength grating in red dashed-line box of (**b**). Scale bar, 1 μm. **d** Transmission spectra at the D1 port when incident from the In1 port as a function of wavelength λ and parameter θ. θ is related to the coupling strength K_{sw} by the equation $K_{sw}=\sin^2(\theta)$. The transmission spectra reveal the boundaries of non-trivial bandgaps within an FSR, marked by black dashed lines. At the bandgap A, edge modes vanish as θ approaches the critical value of 0.364π, while edge modes in bandgap B persist throughout the entire range of θ variation. **e**, **f** Simulated and measured spectra at $\theta = 0.35\pi$ (weak coupling) and $\theta = 0.48\pi$ (strong coupling), respectively. The regions of edge modes are enhanced for the strong coupling case. **g**–**k** Colored infrared images of the electromagnetic field distribution at the points marked in (**e**, **f**), superimposed on SEM images. TPT from topological edge modes (**g**) to randomly distributed bulk modes in bandgap A (**h**), and edge modes (**i**) and forbidden bandgap (**j**) under strong coupling conditions. **k** A unit defect formed by removing a boundary GOR in FTPI. Scale bar, 40 μm. **l** Simulated and measured spectra of a large-scale FTPI consisting of 21 × 21 site GOR lattices at $\theta = 0.48\pi$. **m** Imaged distributions of electromagnetic field. Scale bar, 100 μm. **n** A topological device featuring deliberately introduced complex structural defects arranged in a WLU shape. The inset illustrates the designed layout of these defected lattices. Scale bar: 100 μm.

1-μm-thick silica film was deposited over the entire device using plasma-enhanced chemical vapor deposition (PECVD) to provide protection and encapsulation. To realize the thermo-optical heaters and contact pads, titanium and gold were patterned using UV lithography and deposited via electron beam evaporation. The thermo-optical heaters consisted of a 100-nm-thick titanium layer and a 10-nm-thick gold layer, while the contact pads were composed of a 5-nm-thick titanium layer and a 100-nm-thick gold layer.

Bragg-grating-assisted photonic molecule

By precisely designing the grating period, we can excite counter-propagating higher-order modes in ultra-wide waveguides, in accordance with the Bragg equation $\beta_{FM} + \beta_{SM} = 2\pi/\Lambda$. β_{FM} and β_{SM} are the propagation constants of fundamental- and second-order modes, and Λ is the period of the grating. The coupling rate μ between modes is primarily determined by the power reflectivity $R=\tanh^2(\kappa_g L_g)$, where κ_g and L_g are the coupling strength and length of the grating. Asymmetric peaks in Fig. 3k, l are mainly caused by the frequency mismatch $\delta\omega$ between these two modes. Due to light field distributions of the two modes, phase modulators, such as thermo-optic heaters, can be introduced to compensate for the phase difference accumulated over one round trip of the two modes within the resonator, setting $\delta\omega$ to zero, thereby achieving symmetric peaks. With careful design, this structure is expected to enable precise mode manipulation, such as mode splitting operations on arbitrary modes, to achieve accurate dispersion control.

Infrared image capture

To capture the spatial intensity profiles of the devices, a microscope objective with a 10X magnification was employed to gather the light scattered due to the surface roughness of the GORs. Subsequently, this light was projected onto a high-sensitivity InGaAs camera (Hamamatsu C12741-03, 640 × 512 pixels) via a variable-zoom lens system. The raw images, corresponding to Figs. 5g–k and Fig. 5m, n of the main text are available in Fig. S13.

Data availability

The data generated in this study are provided in the Source Data file. Source data are provided with this paper.

References

1. Rizzo, A. et al. Massively scalable Kerr comb-driven silicon photonic link. *Nat. Photonics* **17**, 992–999 (2023).
2. Kohler, D. et al. Biophotonic sensors with integrated Si3N4-organic hybrid (SiNOH) lasers for point-of-care diagnostics. *Light Sci. Appl.* **10**, 64 (2021).
3. Feldmann, J., Youngblood, N., Wright, C. D., Bhaskaran, H. & Pernice, W. H. P. All-optical spiking neurosynaptic networks with self-learning capabilities. *Nature* **569**, 208–214 (2019).
4. Xia, F., Sekaric, L. & Vlasov, Y. Ultracompact optical buffers on a silicon chip. *Nat. Photonics* **1**, 65–71 (2007).
5. Cui, S. et al. Compact microring resonator based on ultralow-loss multimode silicon nitride waveguide. *Adv. Photonics Nexus* **2**, 046007 (2023).
6. Zhang, L., Jie, L., Zhang, M., Shi, Y. & Dai, D. Ultra-high-Q Silicon Race-track Resonators. *Photonics Res.* **8**, 684–689 (2020).
7. Ji, X. et al. Compact, spatial-mode-interaction-free, ultralow-loss, nonlinear photonic integrated circuits. *Commun. Phys.* **5**, 84 (2022).
8. Xiang, C. et al. 3D integration enables ultralow-noise isolator-free lasers in silicon photonics. *Nature* **620**, 78–85 (2023).
9. Ji, X. et al. Ultra-low-loss silicon nitride photonics based on deposited films compatible with foundries. *Laser Photon Rev.* **17**, 2200544 (2023).
10. Levy, J. S. et al. CMOS-compatible multiple-wavelength oscillator for on-chip optical interconnects. *Nat. Photonics* **4**, 37–40 (2010).
11. Liao, K. et al. Photonic molecule quantum optics. *Adv. Opt. Photonics* **12**, 60–134 (2020).
12. Liang, G. Q. & Chong, Y. D. Optical resonator analog of a two-dimensional topological insulator. *Phys. Rev. Lett.* **110**, 203904 (2013).
13. Marpaung, D., Yao, J. & Capmany, J. Integrated microwave photonics. *Nat. Photonics* **13**, 80–90 (2019).
14. Helgason, ÓB. et al. Surpassing the nonlinear conversion efficiency of soliton microcombs. *Nat. Photonics* **17**, 992–999 (2023).
15. Ye, M., Sun, C., Yu, Y., Ding, Y. & Zhang, X. Silicon integrated multi-mode ring resonator. *Nanophotonics* **10**, 1265–1272 (2021).
16. Sun, C. et al. Key multimode silicon photonic devices inspired by geometrical optics. *ACS Photonics* **7**, 2037–2045 (2020).
17. Sun, C. et al. Integrated mode-transparent polarization beam splitter supporting thirteen data channels. *Photonics Res.* **8**, 978–985 (2020).
18. Zhu, S., Yu, A., Hawley, D. & Roy, R. Frustrated total internal reflection: a demonstration and review. *Am. J. Phys.* **54**, 601–607 (1986).
19. Huntoon, N. R., Christensen, M. P., MacFarlane, D. L., Evans, G. A. & Yeh, C. Integrated photonic coupler based on frustrated total internal reflection. *Appl. Opt.* **47**, 5682–5690 (2008).
20. Bayer, M. et al. Optical modes in photonic molecules. *Phys. Rev. Lett.* **81**, 2582 (1998).
21. Rakovich, Y. P. & Donegan, J. F. Photonic atoms and molecules. *Laser Photonics Rev.* **4**, 179–191 (2010).
22. Bose, R., Cai, T., Choudhury, K. R., Solomon, G. S. & Waks, E. All-optical coherent control of vacuum Rabi oscillations. *Nat. Photonics* **8**, 858–864 (2014).
23. Zhu, R. et al. Full polarization control of photons with evanescent wave coupling in the ultra subwavelength gap of photonic molecules. *Light Sci. Appl* **14**, 114 (2025).
24. Xu, H., Qin, Y., Hu, G. & Tsang, H. K. Breaking the resolution-bandwidth limit of chip-scale spectrometry by harnessing a dispersion-engineered photonic molecule. *Light Sci. Appl* **12**, 64 (2023).
25. Zhang, Y. et al. Miniaturized disordered photonic molecule spectrometer. *Light Sci. Appl* **14**, 144 (2025).

26. Özdemir, Ş, Rotter, S., Nori, F. & Yang, L. Parity–time symmetry and exceptional points in photonics. *Nat. Mater.* **18**, 783–798 (2019).
27. Wang, M. et al. Taming brillouin optomechanics using supermode microresonators. *Phys. Rev. A* **14**, 011056 (2024).
28. Ji, Q.-X. et al. Multimodality integrated microresonators using the Moiré speedup effect. *Science* **383**, 1080–1083 (2024).
29. Yu, S.-P., Lucas, E., Zang, J. & Papp, S. B. A continuum of bright and dark-pulse states in a photonic-crystal resonator. *Nat. Commun.* **13**, 3134 (2022).
30. Yang, C., Hu, Y., Jiang, X. & Xiao, M. Analysis of a triple-cavity photonic molecule based on coupled-mode theory. *Phys. Rev. A* **95**, 033847 (2017).
31. Yu, S.-P. et al. Spontaneous pulse formation in edgeless photonic crystal resonators. *Nat. Photonics* **15**, 461–467 (2021).
32. Lucas, E., Yu, S.-P., Briles, T. C., Carlson, D. R. & Papp, S. B. Tailoring microcombs with inverse-designed, meta-dispersion microresonators. *Nat. Photonics* **17**, 943–950 (2023).
33. Stone, J. R. et al. Wavelength-accurate nonlinear conversion through wavenumber selectivity in photonic crystal resonators. *Nat. Photonics* **18**, 192–199 (2023).
34. Lu, X. et al. Multi-mode microcavity frequency engineering through a shifted grating in a photonic crystal ring. *Photonics Res.* **11**, A72–A79 (2023).
35. Zhang, K. et al. Spectral engineering of optical microresonators in anisotropic lithium niobate crystal. *Adv. Mater.* **36**, 2308840 (2024).
36. Zhang, M. et al. Electronically programmable photonic molecule. *Nat. Photonics* **13**, 36–40 (2019).
37. Tao, Z. et al. Versatile photonic molecule switch in multimode microresonators. *Light Sci. Appl.* **13**, 51 (2024).
38. Woska, S., Rietz, P., Karayel, O. & Kalt, H. Tunable coupling of chip-scale photonic molecules via thermal actuation. *Opt. Mater. Express* **11**, 3194–3207 (2021).
39. Wang, J., Liu, K., Isichenko, A., Rudy, R. Q. & Blumenthal, D. J. Integrated programmable strongly coupled three-ring resonator photonic molecule with ultralow-power piezoelectric control. *Opt. Lett.* **48**, 2373–2376 (2023).
40. Zheng, S. N. et al. Microring resonator-assisted Fourier transform spectrometer with enhanced resolution and large bandwidth in single chip solution. *Nat. Commun.* **10**, 2349 (2019).
41. Hafezi, M., Demler, E. A., Lukin, M. D. & Taylor, J. M. Robust optical delay lines with topological protection. *Nat. Phys.* **7**, 907–912 (2011).
42. Ma, A. et al. Anisotropic quantum transport in a programmable photonic topological insulator. *Optica* **11**, 1533–1539 (2024).
43. Huang, J. et al. Integrated optical entangled quantum vortex emitters. *Nat. Photonics* **19**, 471–478 (2025).
44. Harari, G. et al. Topological insulator laser: theory. *Science* **359**, eaar4003 (2018).
45. Zhang, Z., Delplace, P. & Fleury, R. Superior robustness of anomalous non-reciprocal topological edge states. *Nature* **598**, 293–297 (2021).
46. Leykam, D., Mittal, S., Hafezi, M. & Chong, Y. D. Reconfigurable topological phases in next-nearest-neighbor coupled resonator lattices. *Phys. Rev. Lett.* **121**, 023901 (2018).
47. Ao, Y. et al. Topological phase transition in the non-Hermitian coupled resonator array. *Phys. Rev. Lett.* **125**, 013902 (2020).
48. Dai, T. et al. Topologically protected quantum entanglement emitters. *Nat. Photonics* **16**, 248–257 (2022).
49. Bai, S. et al. Integrated high-Q Fabry-Pérot Cavity at 780 nm with ultrabroad operating bandwidth and high fabrication tolerance. *Laser Photon Rev.* **19**, e00796 (2025).
50. Prokoshin, A., Gehl, M., Madaras, S., Chow, W. W. & Wan, Y. Ultra-narrow-linewidth hybrid-integrated self-injection locked laser at 780 nm. *Optica* **11**, 1024–1029 (2024).
51. Morrison, B. et al. Compact Brillouin devices through hybrid integration on silicon. *Optica* **4**, 847–854 (2017).
52. Bandres, M. A. et al. Topological insulator laser: experiments. *Science* **359**, eaar4005 (2018).
53. Hashemi, S. D. & Mittal, S. Floquet topological dissipative Kerr solitons and incommensurate frequency combs. *Nat. Commun.* **15**, 9642 (2024).
54. Mittal, S. et al. Photonic quadrupole topological phases. *Nat. Photonics* **13**, 692–696 (2019).

Acknowledgements

The authors would like to acknowledge Westlake Center for Micro/Nano Fabrication and Instrumentation, Service Center for Physical Sciences at Westlake University, and ZJU Micro-Nano Fabrication Center at Zhejiang University for the facility support.

Author contributions

C. S. came up with the device design. C. S. and K.B. carried out the device simulations and testing. K. B. and B. T. fabricated the devices. B. S., X. Y., Z. C., Y. T., Q. D., Y. W., L. L., R. T., Z. L., K. L., and Y. S. contributed to device characterization and testing. W. S., M. Q., H. L., and L. L. supervised and coordinated the project. All authors contributed to technical discussions and writing the paper.

Funding

"Pioneer" and "Leading Goose" R&D Program of Zhejiang Province (2024SDXHDX0005); National Natural Science Foundation of China (62205274, 62175202); National Key Research and Development Program of China (2024YFB2808700); "Pioneer" R&D Program of Zhejiang (2025C01002); Key Project of Westlake Institute for Optoelectronics (2023GD003/110500Y0022303); Zhejiang Provincial Natural Science Foundation of China (LD22F040002).

Competing interests

The authors declare no competing interests.

Additional information

Supplementary information The online version contains supplementary material available at https://doi.org/10.1038/s41467-026-77489-x.

Correspondence and requests for materials should be addressed to Chunlei Sun, Min Qiu, Hongtao Lin or Lan Li.

Peer review information *Nature Communications* thanks the other anonymous reviewer(s) for their contribution to the peer review of this work. A peer review file is available.